

Diffusion MRI: Applications Outside the Brain

24

Ricardo Donners^a, Mihaela Rata^b, Neil Peter Jerome^c, Matthew Orton^d, Matthew Blackledge^d,
Christina Messiou^b, and Dow-Mu Koh^b

^aDepartment of Imaging, University Hospital of Basel, Basel, Switzerland ^bDepartment of Radiology, Royal Marsden Hospital, Sutton, United Kingdom ^cDepartment of Circulation and Medical Imaging, Norwegian University of Science and Technology, Trondheim, Norway ^dDivision of Radiotherapy and Imaging, Institute of Cancer Research, Sutton, United Kingdom

24.1 Introduction

Diffusion imaging is a noninvasive technique that yields information on tissue structure without the need for exogenous contrast administration or the use of ionizing radiation. The technique can be used to visualize and quantify differences in water mobility in human tissues, which are composed of approximately 70% water. In the body, water mobility (diffusion) is impeded in regions with increased tissue cellularity, cellular membrane integrity, fluid viscosity, and extracellular space tortuosity, which lead to a higher observed signal intensity on diffusion-weighted imaging (DWI) compared to tissues where water can move freely. Although the first clinical use of DWI was in the brain, advances in hardware and scanning sequences have largely overcome the challenges of implementing the technique in extracranial applications, both at 1.5 and 3 T. DWI has become a core element of many standard body MRI protocols for disease detection, characterization, and response assessment. Quantification of water mobility using the apparent diffusion coefficient (ADC) with a simple monoexponential model, or via more complex measurements using bi-exponential or non-Gaussian models, are still being refined. In this chapter, we provide readers with a perspective of the technical development of body diffusion imaging, its implementation on current Magnetic Resonance Imaging (MRI) platforms, approaches to the quantification of diffusion, applications of DWI and diffusion mapping, evolving developments.

24.2 Principles of diffusion imaging as applied in the body

24.2.1 General considerations

The dependency of the MRI signal on molecular water diffusion was described as early as 1950 [1]. The principle of adding diffusion-sensitizing magnetic field gradients, known as “diffusion gradients,” to a T_2 -weighted pulse sequence to impart diffusion-weighted contrast into an MR image was described in 1965, and still forms the basis for many diffusion measurements today [2]. The most basic diffusion sequence involves the addition of two diffusion gradients. The first gradient dephases the magnetic

spins of the protons in water molecules by adding a spatially dependent phase shift. The second gradient is of the same magnitude and duration, but with the opposite direction to the first gradient, thus reversing the phase shift. Since there is molecular motion in the time between the application of the two diffusion gradients, spins moving during this period experienced a different magnetic field during the rephasing and rephasing gradients, leading to an overall dephasing and signal loss. Increased molecular motion (diffusion) leads to a larger signal decrease, which results in the diffusion-weighted image contrast. By contrast, impeded or restricted water diffusion leads to less signal attenuation and relatively preserved high signal. It should be noted that, in the clinical context, the term “restricted” diffusion is commonly used to refer to decreased diffusivity from any cause. However, diffusion restriction technically only refers to molecules encountering physical boundaries such as cell membranes leading to the tapering of diffusion-related signal loss with increasing diffusion time. This phenomenon would not be encountered if there was simply decreased (but unrestricted) diffusivity as it would occur in highly viscous fluids. This distinction is presently not made in clinical interpretation.

The amount of signal attenuation at a particular location within a diffusion-weighted image depends on two quantitative parameters: (1) the “ b -value,” which summarizes the gradient amplitude, duration, and the time interval between the paired diffusion sensitizing gradients, and (2) the “ADC,” which is an empirical parameter that describes the mobility of water at that location. For systems where the distribution of proton displacements in a given time is Gaussian, the signal decay as a function of b -value is a monoexponential curve, and the rate constant of this decay is the diffusion coefficient. In biological systems the diffusion environment is more complex, so to indicate this complexity the rate constant of a monoexponential fit to the signal decay curve is known as the “ADC.” Given a particular b -value and ADC, signal (S) within a diffusion-weighted image is attenuated according to a monoexponential decay model, with an exponent equal to the negative product of these parameters. If S_0 is the MRI signal at baseline, the DWI signal is equal to

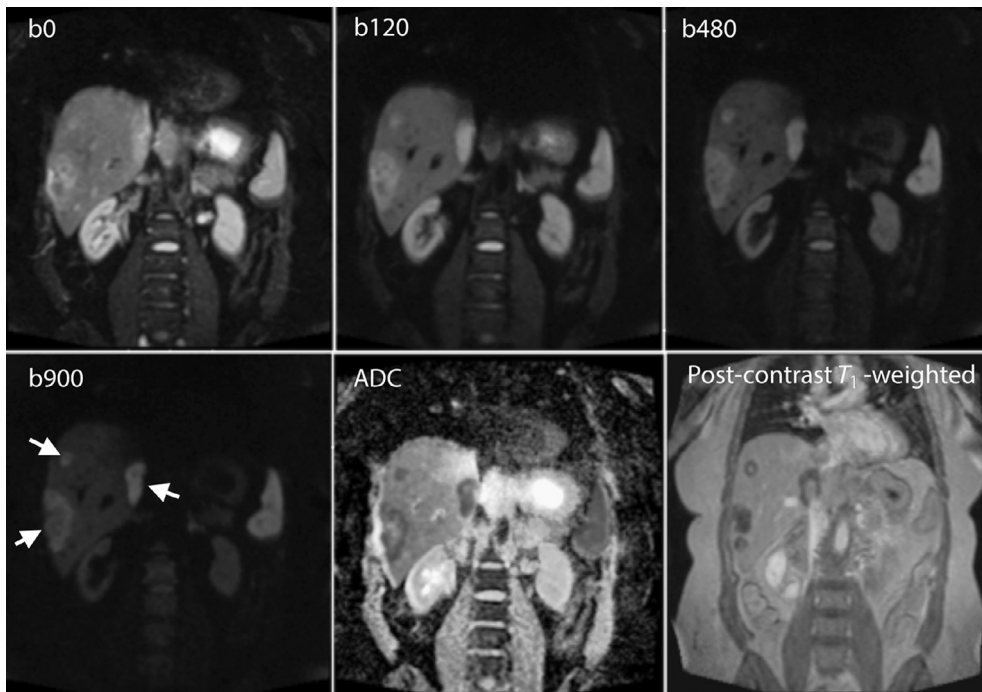
$$S = S_0 e^{-b \text{ ADC}}$$

Typical b -values for body imaging range from 0 to 1000 s/mm², although higher b -values up to 4000 s/mm² have been applied in specific disease contexts. Using higher b -values is desirable to enhance diffusivity-based tissue contrasts but decreases the image signal to noise ratio (SNR). Typical ADCs encountered in the human body range from 0.5–3.0 × 10^{−3} mm²/s. Although the relationship between ADC value and tissue cellularity is complex and varies between disease settings and low diffusivity can also be seen in viscous fluids, a lesion with low ADC value (e.g., between 0.5–1.0 × 10^{−3} mm²/s) is often more cellular compared with adjacent tissues (Fig. 24.1).

24.2.2 Technical considerations

24.2.2.1 Echo-planar imaging technique

One of the key considerations of performing diffusion imaging in the body is the need to overcome the effects of motion arising from the heart, bowel, blood flow, respiration, and gross patient movement. In this regard, the acquisition of diffusion images needs to be fast to be motion-robust. Single-shot echo-planar imaging (SS-EPI) is now the most widely used diffusion imaging technique, as physiological effects of motion are small within the rapid readout of the sequence (typically less than 100 ms per image). This image readout technique is commonly used as part of a spin echo pulse sequence, and the long echo time (T_E) required to obtain the diffusion sensitization gives the overall image a T_2 -weighted

**FIG. 24.1**

Abdominal diffusion imaging of a 48-year-old female patient with hepatic metastasis of colorectal cancer. Coronal EPI DW images of the abdomen with different b -values acquired during free breathing (b_0 , b_{120} , b_{480} , b_{900}), and the corresponding ADC map calculated using all the b -values. Three discrete metastases can be seen (arrows). The T_1 -weighted post-gadolinium image shows partial enhancement of the metastases. The mean ADC value for the nonnecrotic areas of liver metastases is $0.8\text{--}0.9 \times 10^{-3} \text{ mm}^2/\text{s}$, while the ADC of normal liver is $1.2 \times 10^{-3} \text{ mm}^2/\text{s}$.

contrast as well. SS-EPI diffusion imaging is highly sensitive to magnetic field inhomogeneities, susceptibility effects caused by tissue interfaces, and eddy-currents induced in the coils by fast switching imaging gradients, sometimes leading to severe geometric distortions. A major technical breakthrough, making diffusion imaging outside the brain practicable, was the development of parallel imaging and partial Fourier reconstruction for faster readout of undersampled data using shorter echo-trains [3]. Despite these advances in image acquisition, however, the SS-EPI diffusion imaging technique is still prone to image distortion, which must be accounted for in the radiological interpretation of diffusion-weighted images. SS-EPI diffusion imaging is most frequently performed in free-breathing, although motion-controlled acquisitions (breath-hold or respiratory triggered) can be considered in selected areas [4].

Fat suppression is required at image acquisition for robust diffusion imaging. This is commonly achieved using a spectral adiabatic inversion recovery (SPAIR) technique for smaller field of view (FoV) imaging [5], and using short-tau inversion recovery (STIR) technique over larger imaging FoVs. Diffusion imaging sequences should be optimized by an expert physicist or technologist to maximize image SNR and to minimize image artifacts, to ensure reliable and consistent performance.

24.2.2.2 Non-EPI diffusion imaging

With improvements in imaging hardware and image acquisition acceleration techniques, there has been increasing interest in using non-EPI diffusion techniques in the body. Diffusion-sensitizing gradients may be added to turbo spin echo (TSE) or fast spin echo (FSE) sequences. The 180° refocusing pulse of these sequences reduces phase shifts, reducing the sensitivity to susceptibility effects in tissues, hence reducing image distortion, which can be advantageous at anatomical areas with gas-tissue interfaces. The acquisition times remain short but are longer than for SS-EPI (approximately 300ms per image). Potential issues related to the associated longer overall image acquisition times, lower image SNR, and motion blurring have reduced the wider adoption of these non-EPI techniques. Segmented, parallel and non-Cartesian readout models have been used to increase image SNR and motion robustness, such as periodically overlapping parallel lines read-out (PROPELLER), split-echo PROPELLER (SPICE), and self-navigated interleaved spirals (SNAILS) acquisitions [6, 7].

24.2.2.3 Reduced FoV diffusion imaging

One of the strengths of MRI is the ability to interrogate specific organs and structures using reduced FoV imaging to improve image spatial resolution within the same scan time. This is frequently employed when using conventional morphological imaging to improve disease visualization.

For diffusion imaging, a limited FoV can be achieved by inner volume imaging (IVI), where two or three perpendicularly oriented gradients excite only the intersecting voxels; or outer volume suppression (OVS), where the signal of outer tissues is nulled [8, 9]. Variants of IVI have been developed by the major vendors: FOCUS (General Electric), ZOOMit (Siemens), and iZOOM (Philips). Reduced FoV imaging has been shown to improve image quality compared with larger FoV diffusion imaging in the spinal cord, prostate, pancreas, breast, head and neck, and cervical cancer [9–13]. As an alternative to reduced FoV diffusion imaging, segmented multishot-EPI can also be applied to decrease image distortion and increase acquisition matrix size [14] (Fig. 24.2). Such techniques are increasingly applied to improve the quality of targeted diffusion imaging across the body. Early studies suggested some discrepancies in quantitative ADC values using limited FoV compared with conventional larger FoV imaging, but more recently equivalent ADC measurements were reported in larger studies [11, 13].

24.2.2.4 Computed DWI

The use of higher b -values (i.e., higher diffusion weighting) results in greater suppression of the MR signal from normal tissues and can, therefore, increase lesion conspicuity on DWI. However, using higher b -values increases the sensitivity to susceptibility artifacts and image distortion, and decreases

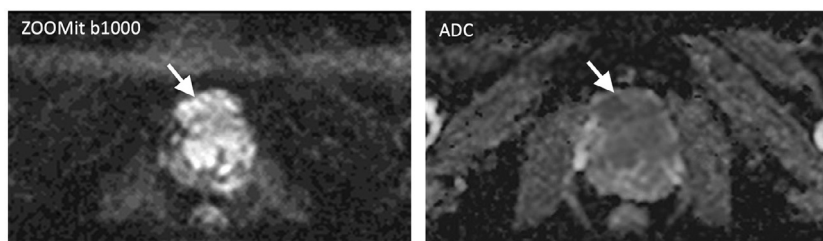


FIG. 24.2

Limited field-of-view imaging. Using an inner volume excitation technique (ZOOMit) at a b -value of 1000 s/mm^2 , the prostate gland is well seen showing a tumor (arrows) in the transitional zone, with a high signal intensity due to reduced diffusion, and low ADC values.

SNR and image quality. Computed DWI is an image postprocessing technique that can be applied to generate a synthetic image simulating any higher b -value image from the quantitative ADC map obtained using images with lower diffusion weightings, a strategy that can overcome the aforementioned drawbacks. In a phantom study, computed DWI of a higher b -value yielded higher SNR than images acquired using an equal b -value, especially with b greater than 840 s/mm^2 [15]. Computed DWI at a b -value of 2000 s/mm^2 resulted in higher diagnostic accuracy than acquired $b = 900 \text{ s/mm}^2$ images for metastatic bone disease detection using whole-body diffusion (WB-DWI) while maintaining good image quality [15, 16] (Fig. 24.3).

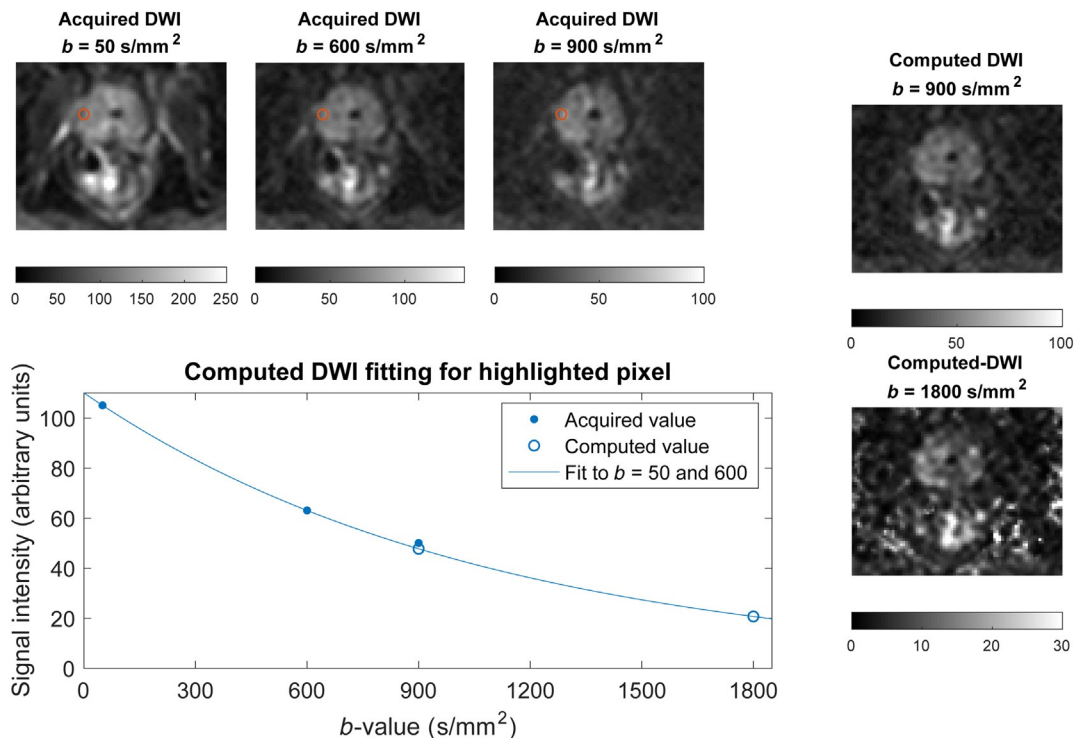


FIG. 24.3

Example showing the computed DWI technique applied to generate high b -value diffusion-weighted images in a 68-year-old man with prostate cancer. The three top left images are diffusion-weighted images acquired at $b = 50, 600$, and 900 s/mm^2 . The plot shows values for the pixel highlighted in red. The curve in this plot is derived by fitting a mono-exponential function to the first two b -values (50 and 600 s/mm^2 , filled circles), which is used to generate computed values at two higher b -values (900 and 1800 s/mm^2 , open circles). The unfitted value at $b = 900 \text{ s/mm}^2$ is also shown for reference. Application of this fitting process to every pixel can be used to synthesize an image at any b -value, and the images in the right-hand panels show images computed at $b = 900$ and 1800 s/mm^2 . Comparison of the acquired and computed images at $b = 900 \text{ s/mm}^2$ indicates a good agreement, while the computed image at $b = 1800 \text{ s/mm}^2$ demonstrates extrapolation to a diffusion weighting that may be difficult to acquire in practice.

24.2.2.5 Diffusion imaging at 1.5 T versus 3 T

Imaging at 3 T has the potential to increase image SNR over 1.5 T diffusion imaging, though quantitative measurements should remain constant as the field strength does not affect molecular mobility. However, general considerations for 1.5 versus 3 T imaging and issues associated with higher field strength also apply to diffusion imaging [17]. Particular challenges of diffusion imaging at 3 T have increased eddy currents from the rapidly switching gradients used in EPI, and higher impact of magnetic susceptibility variations of neighboring tissues causing image distortion, misregistration, and overall degradation of image quality [5]. Furthermore, uniform fat suppression can be more difficult to achieve due to increased B_1 field inhomogeneities at 3 T, which leads to chemical shift and ghosting artifacts [5]. The decreased image quality of 3 T versus 1.5 T diffusion imaging has been reported in phantom studies [18, 19], although increased lesion conspicuity was also observed at 3 T [20, 21]. One of the recent implementations at 3 T to improve B_1 field inhomogeneity is the use of image-based shimming techniques, which can significantly improve the quality of extracranial diffusion studies, especially over large FoVs in the body [22].

24.3 Quantitative diffusion mapping

Qualitative visual assessment of signal intensities is currently the mainstay for the interpretation of diffusion imaging in clinical practice. The radiologist utilizes all available MRI sequences and arrives at a diagnostic conclusion by a cognitive appraisal of signal contrasts and tissue morphology. The qualitative approach is commonly used in most clinical settings, but is subjective and has several limitations including interoperator and interscanner variability of disease assessment, SNR floors, and interpretation errors due to confounders from competing brightness effects from different contrast mechanisms (e.g., “ T_2 shine-through”) [23]. These limitations can be mitigated by quantitative analyses of water mobility, improve the characterization of lesion heterogeneity, confirm diffusivity changes occult to the naked eye, and increase overall objectivity.

24.3.1 Quantitative measurements using the monoexponential model

The most widely used quantitative parameter, derived by using a monoexponential model for the measured DWI signal with two or more b -values, is the ADC. Most MRI systems provide an in-line calculation of an ADC map. By drawing regions of interest (ROIs) on this map, the ADC value of tissues can be recorded. In clinical practice, it is the mean ADC across an ROI that is most frequently reported, although other ADC histogram parameters are also being used; the relative strengths and weaknesses of these are discussed in the following section (Fig. 24.4).

24.3.1.1 Mean ADC

Studies have provided biological validation showing an inverse correlation between the ROI-derived mean ADC value and the tissue cellularity and tumor grade [24–26]. In clinical studies, an excellent interreader agreement was reported for the mean ADC [27]. The mean ADC value has approximately 3%–6% interstudy variation, increasing with smaller volume measurements. Besides, intervender measurement variability of a similar magnitude can also contribute to the measurement variations [28–31]. Overall, changes of mean ADC value greater than 15%–30% from comparable ROIs may be considered as confidently detectable.

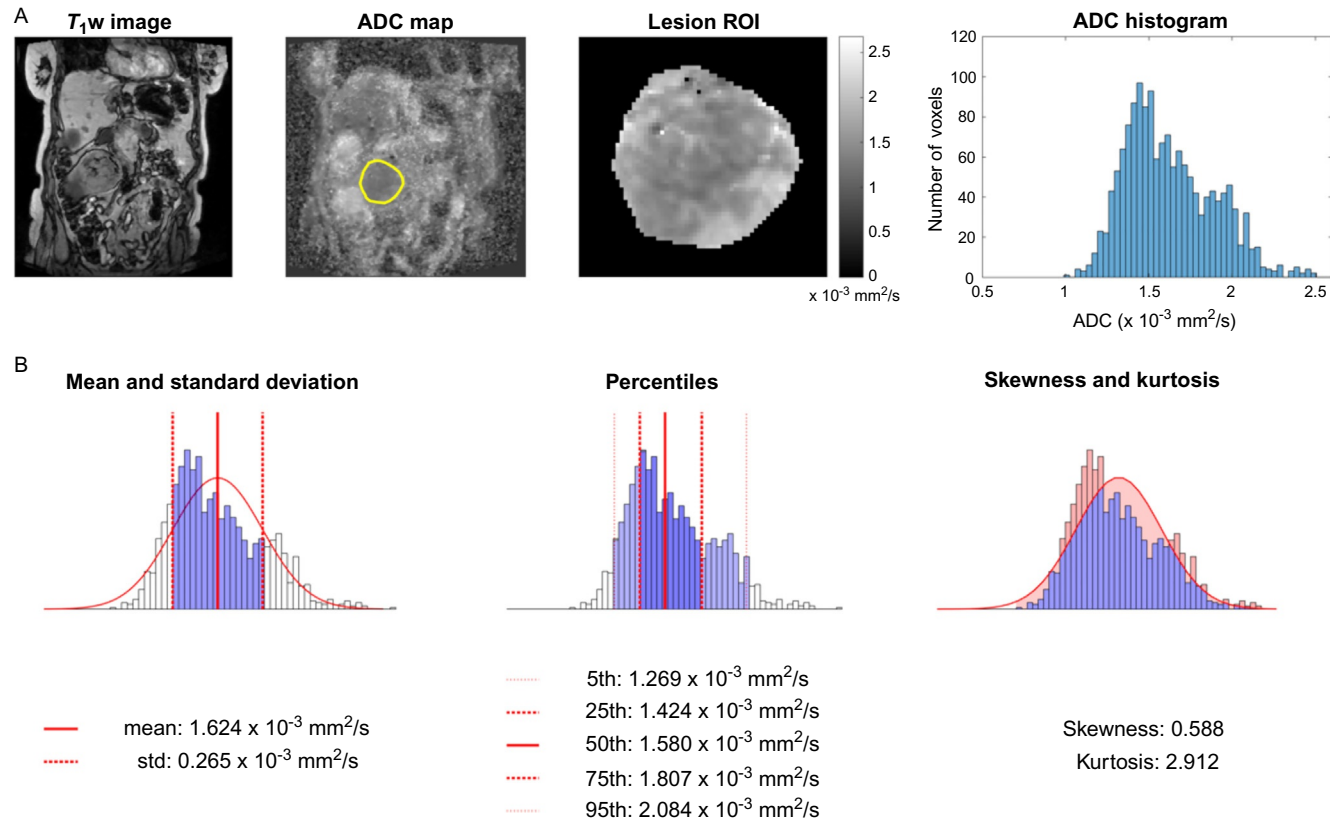


FIG. 24.4

Renal cell carcinoma in a 72-year-old man. (A) (left to right) T_1 -weighted image, and ADC map from diffusion-weighted images (10 b -values, 0–1000s/mm²). The tumor appears dark on the ADC map due to impeded water diffusion (ROI shown in outline). The individual voxel ADC values from the tumor are extracted to give the ADC histogram. (B) Histogram analysis is performed to generate: (Left) The mean and standard deviation (assuming normal distribution) as summary parameters, but which can be affected by outliers. (Center) The median (50th percentile) is less sensitive to outliers and may be a better summary parameter. Using other percentiles values, such as interquartile range, gives a measure of spread. The lower percentiles, down to 5th percentile, may be informative in oncological diffusion imaging, since these correspond to more impeded water diffusion which is linked to higher cell density. Minima (and maxima) of the histogram have large statistical variability and should be avoided. (Right) Higher moments of the histogram can be calculated, such as skewness (3rd moment) and kurtosis (4th moment). Positive skewness indicates a longer right-side tail, with negative skewness vice versa (symmetrical distributions have zero skewness). Kurtosis values above 3 indicate both tails are heavier than a normal distribution, and values below 3 indicate lighter tails than a normal distribution.

24.3.1.2 Minimum and maximum ADC values, and ADC percentile values

By hypothesis, the area with minimum ADC value should correspond to the area of highest cellularity, thus indicating the most viable or most aggressive tumor. In contrast, the maximum ADC should indicate the least cellular areas, thus may help identify early response to therapy associated with cell death and decreased cellularity. However, both the minimum and maximum ADC are samples arising from the tails of the ADC histogram, which are subject to larger sampling variability than other statistical properties (e.g., the mean), and thus show poor measurement repeatability. For these reasons, it may be more robust to report on the 5th and 95th percentiles to reflect changes in the lower and upper ranges of ADC [32]. Measures of location and spread from assessing percentiles use the median (50th percentile), and interquartile range (75th–25th percentile).

24.3.1.3 Skewness and kurtosis

The skewness and kurtosis of diffusion measurements are related to the shape of the histogram of ADC values. Skewness reflects the asymmetry of the ADC distribution; a positive skewness indicates a long right-hand tail of the ADC distribution. Kurtosis is related to the prevalence of extreme values in the ADC distribution, and kurtosis values greater than three are associated with longer histogram tails than a Gaussian distribution. Both parameters usually behave in a coherent pattern in cancers: a large skewness and kurtosis of the ADC distribution are often present in untreated, highly cellular, and viable tumor. A decrease of skewness and kurtosis throughout treatment is associated with therapy response [33]. However, similar to a minimum and maximum ADC, skewness, and kurtosis show poor measurement repeatability with high interobserver and intraobserver variance [34]. For these reasons, the visual appraisal of the histogram distribution may be more practical than the absolute quantification of the skewness and kurtosis values.

24.3.2 Nonmonoexponential quantitative measurements

The observed signal decay of the diffusion signal in tissues is in practice nonmonoexponential to a varying degree, reflecting the complexity of tissue organization. Hence, although the simple ADC measurement is robust in summarizing complex tissue diffusion properties [35], there is a significant interest in deploying more sophisticated diffusion models to derive additional parameters that may improve disease characterization. These nonmonoexponential diffusion models make different assumptions about the tissue microstructure and the three most widely used models of this sort—the IVIM model, the stretched-exponential model, and the diffusion-kurtosis model—are briefly reviewed in the following section.

24.3.2.1 IVIM modeling of diffusion signals: D , D^* , and f

The intravoxel incoherent motion (IVIM) model is a description of the diffusion signal that accounts for two distinct compartments of water molecules within a voxel during imaging, with separate signal attenuation characteristics. With diffusion sensitizing gradients over a certain threshold value, changes in signal intensity with b -value are mostly related to “true” (random) diffusion, labeled by the coefficient D , and are modeled as an exponential decay similar to the ADC model. The second component describes signals arising from water molecules undergoing convective transport in the capillaries. Under the assumption of the random orientation of vessels within each voxel, this motion also leads to signal dephasing and, therefore, signal loss, which manifests as a fast pseudodiffusion process. This can also be modeled with an exponential decay, whose rate constant is the pseudodiffusion coefficient D^* .

The diffusion signal attenuation at low b -values, commonly less than 200 s/mm^2 , reflects both compartments. Consequently, low b -value signal attenuation is greater than expected when considering only “true” diffusion effects. Thus, using the ADC model in the presence of pseudodiffusion would lead to values higher than expected for the random diffusion component alone [36, 37]. Under the assumptions of the IVIM model, the diffusion signal is the sum of true diffusion (D) and pseudodiffusion components (D^*) and their relative contribution is quantified by the pseudodiffusion fraction (f) which is reflective of a perfusion contribution [37, 38]. The bi-exponential IVIM signal function can be expressed as follows:

$$S = S_0 \left(f e^{-b(D+D^*)} + (1-f) e^{-bD} \right)$$

To apply this model effectively, measurements at multiple b -values are necessary. Although the ideal number and location depend on the organ and pathology, between 5 and 16 b -values are commonly used. Acceptable repeatability and variability have been reported for D , but f and D^* have much larger variations [39, 40]. IVIM diffusion imaging has shown promising results on a cohort basis for imaging of tumors of the kidney, head and neck, pancreas, breast, bladder, and liver as well as functional imaging of the kidneys [41–46], but its applicability on a per-patient basis requires further investigation.

24.3.2.2 Stretched exponential model: α , DDC

In tissues, multiple processes contribute to water diffusion within a voxel, leading to nonmonoexponential signal attenuation by considering these processes as relating to microscopic heterogeneity. The signal can be modeled as a sum of many Gaussian diffusion-related signals decays at different rates. The stretched exponential can be used to model the overall signal decay as arising from a continuous distribution of decay rates [47]. This is achieved by including a dimensionless stretching term α in the diffusion attenuation model, which accounts for deviations from monoexponential behavior, and is constrained to values between 0 and 1:

$$S = S_0 \exp[-(b \times DDC)^\alpha]$$

where DDC is the distributed diffusion coefficient. A α value of 1 indicates a Gaussian diffusion process with homogenous diffusion coefficients within the voxel. Values of α which are less than 1 indicate increasing heterogeneity. The DDC is a metric of the tissue diffusivity derived from the stretched-exponential function [47]. Stretched exponential parameters have been reported to aid the characterization and staging of diffuse liver disease, bladder, ovarian, and breast cancers [46, 48–51].

24.3.2.3 Diffusion kurtosis imaging: K , D

Another approach to model diffusion signal attenuation to reflect non-Gaussian diffusion caused by microscopic heterogeneity is diffusion kurtosis imaging (DKI), which uses ultrahigh b -values (greater than 1500 s/mm^2), to sensitize the signal to a greater range of tissue properties. In tissues, the increased mobility of extracellular water compared to intracellular water implies that at very high b -values the extracellular water signal is attenuated more than the intracellular water, and the DKI approach is designed to sensitize the measurement to such microstructural properties [50]. Using the DKI model, the parameters derived include ADC (D_{app}) and the apparent diffusion kurtosis, K_{app} . The DKI signal function is expressed as follows:

$$S = S_0 \left(e^{-bD + b^2 D^2 K/6} \right)$$

K_{app} characterizes the degree of non-Gaussian diffusion. A value close to 0 reflects Gaussian diffusion; values greater than zero are indicative of a signal decay that is less attenuated at high b -values than monoexponential tissues with the same D_{app} [50]. For example, K_{app} is significantly larger in prostate cancer than normal parenchyma [51], which is indicative of altered tissue structure in carcinoma.

24.3.3 Whole-body quantitative diffusion measurements: Diffusion volume, global ADC

Whole-body diffusion-weighted imaging, WB-DWI, was introduced in 2004 and has evolved to become a powerful diagnostic tool for disease detection and staging. It is especially advantageous for evaluating systemic bone diseases such as metastatic breast and prostate cancer, as well as multiple myeloma [52]. WB-DWI is typically performed by the sequential acquisition of 4–6 axial image stacks, each providing a field-of-view of approximately 20cm in the head-foot direction. These images are combined into a total-body diffusion study in postprocessing and can be viewed using volumetric displays such as a maximum intensity projection (MIP). As with anatomically-specific diffusion examinations, the highly cellular tumor is highlighted while healthy background tissue is suppressed, creating high lesion-to-background contrast. This contrast may be further increased by utilizing calculated ultrahigh b -values, facilitating lesion segmentation [15, 53]. Disease segmentation based on the disease signal intensity allows estimation of the total disease burden, termed the total diffusion volume (tDV), which is a promising marker for disease prognosis and response assessment. For example, in metastatic castration-resistant prostate carcinoma (mCRPC) patients, the tDV showed an inverse correlation with overall survival [54]. A 40%–50% tDV decrease during oncological therapy may indicate therapy response [53, 55]. In addition, the ADC values associated with entire segmented disease volume (global ADC) can also inform on disease cellularity (Fig. 24.5). A mean gADC increase of 30% or more may be indicative of therapy response. tDV and global ADC (gADC) have also been shown to have good measurement reproducibility and interreader agreement [33, 34, 54, 56].

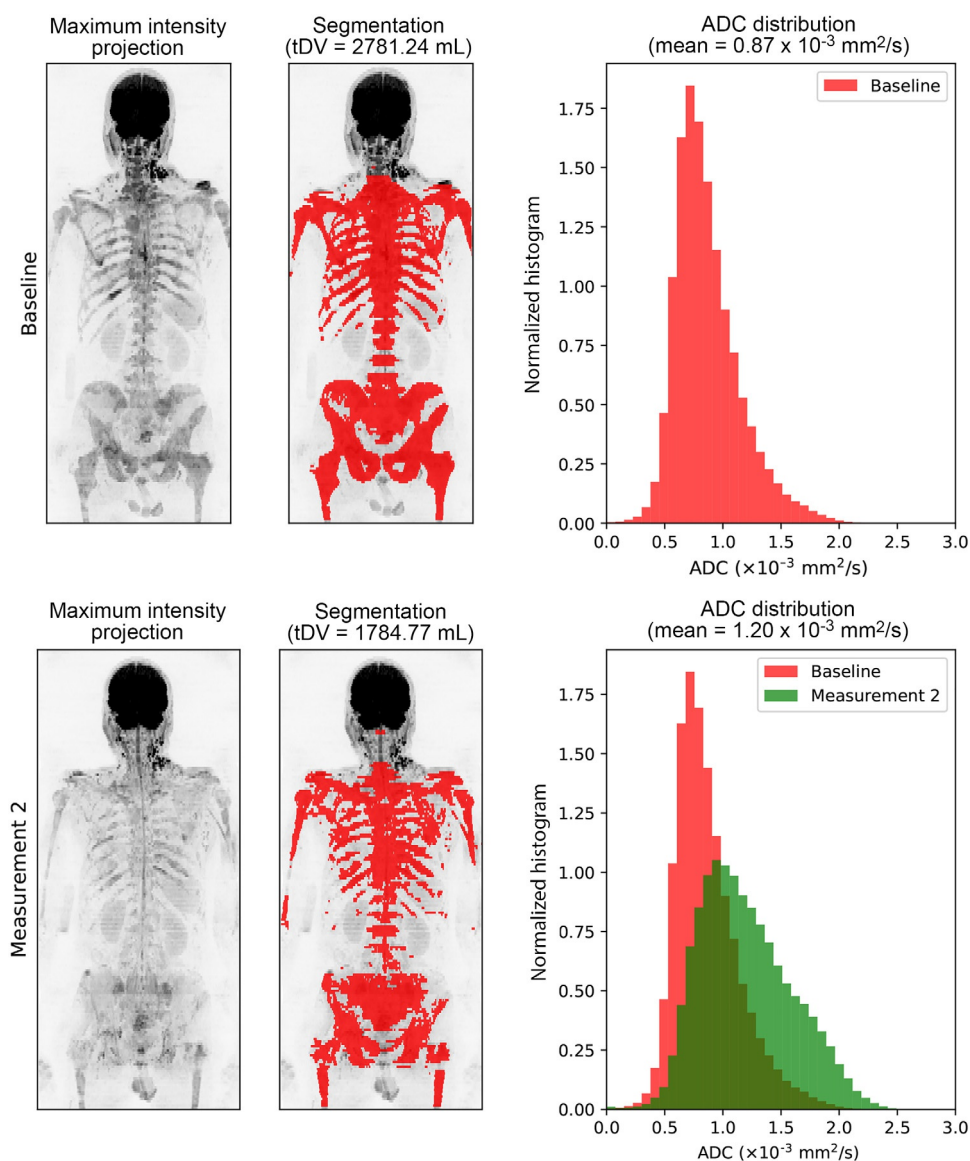
24.4 Clinical applications

Diffusion imaging has become a standard MR sequence regardless of body region and even in a whole-body setting. It is currently employed in many nononcological and oncological applications. The reader should bear in mind the strengths and limitations of the technique, as well as the need to combine diffusion imaging with anatomical MRI sequences for optimal interpretation. In the following sections, we survey the established deployment of extracranial diffusion imaging in clinical practice, focusing on indications where there is significant evidence for its added value.

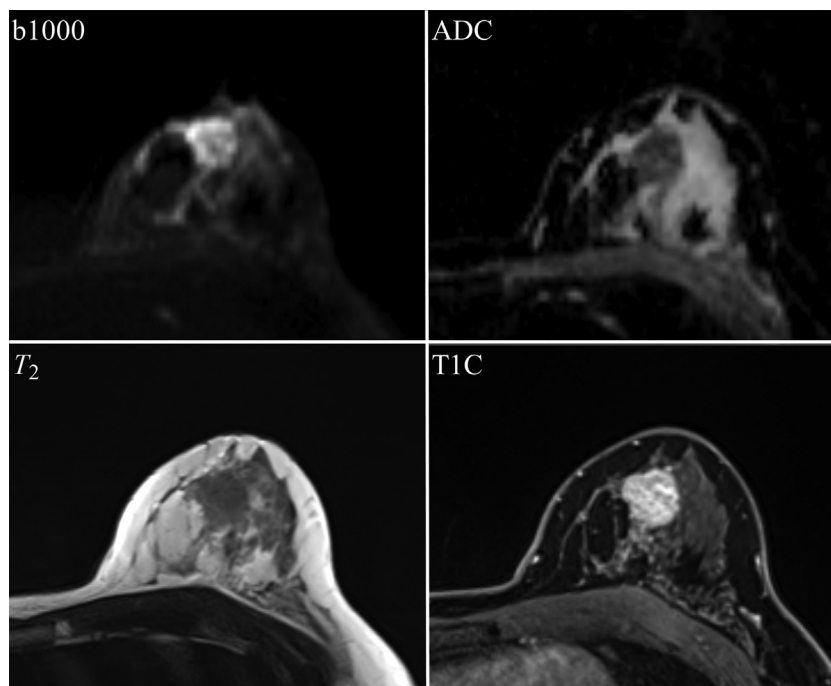
24.4.1 Breast cancer

24.4.1.1 Disease detection

Malignant breast lesions show impeded diffusion compared with normal fibro-glandular tissue [57]. A metaanalysis evaluating 964 breast lesions, 615 malignant and 349 benign, demonstrated a combined sensitivity of 84% and specificity of 79% for discriminating between malignant and benign lesions based on DWI [58]. Diffusion imaging increases the diagnostic accuracy of breast MRI complementary

**FIG. 24.5**

An elderly male with prostate carcinoma with diffuse bone metastases. Inverted maximum intensity projections (MIP) and corresponding segmentation of the total diffusion volume (tDV in red) of the metastatic bone disease derived from whole-body diffusion imaging. Measurement 2 was performed after chemotherapy. When comparing the ADC histogram derived from the tDV at baseline and after chemotherapy, an increase in ADC as well as a reduction of skewness and kurtosis is observed, consistent with response to therapy.

**FIG. 24.6**

A 38-year-old woman with breast cancer. A 2 cm tumor is visible in the left breast showing impeded diffusion (b1000 diffusion-weighted image), low ADC value (ADC image), low T_2 signal intensity (T_2 image) and avid contrast enhancement (T1C image) typical of a breast carcinoma.

to contrast-enhanced imaging [59] (Fig. 24.6) and may reduce unnecessary biopsies for mammogram screen-detected lesions [60]. Quantitative ADC cut-off values to discriminate malignant from benign lesions are not consistent, due to ADC dependence on chosen b -values and the lack of a universally accepted imaging standard. However, the sensitivity and specificity for the detection of malignancy do not appear affected by different b -values in clinical use [61] or prior intravenous contrast administration [62].

24.4.1.2 Disease characterization

The menstrual cycle does not significantly affect the ADC values of glandular tissue [63]. However, the ADC value is reduced in lactating breasts [64]. ADC correlates with breast density, thus breast tissue ADC values are lower in postmenopausal than premenopausal women [55]. In either case, the normal range of glandular tissue remains higher than in malignancies, thus the diagnostic performance of ADC is not compromised. Ductal carcinoma in situ (DCIS) lesions are associated with higher ADC values than invasive cancer, and lesions that become invasive cancers showed lower ADC values than those that remained as DCIS [65–67]. Lower ADC values in breast cancer are correlated with higher proliferation and cellularity. Although a strong negative correlation between ADC value and tumor grade was reported [63, 65], the ADC correlations with other known prognostic factors remain inconsistent [64].

24.4.2 Head and neck cancers

24.4.2.1 Disease detection

Malignancy is associated with impeded diffusion, leading to high signal on DWI and low ADC. Proposed ADC cut-offs discriminating malignant from benign lesions range between $1.15\text{--}1.3 \times 10^{-3} \text{ mm}^2/\text{s}$ with reportedly high diagnostic accuracy (86% to 96%) using SS-EPI DWI and b -values of 0 and 1000 s/mm^2 [68–70].

24.4.2.2 Response assessment

Complete therapy response was associated with significant ADC increase, while therapy failure was correlated with ADC decrease throughout chemoradiation of squamous cell cancer [71, 72]. One study observed that a lower ADC increase at 2 and 4 weeks after treatment was associated with higher recurrence rates [73]. Diffusion imaging can help to distinguish between posttherapeutic tissue changes and disease recurrence, the latter being more likely to show impeded diffusion against the reactive, inflammatory tissue changes due to an increase in cellularity [74]. Low pretreatment ADC values were associated with better therapy response and longer overall survival than high ADC values [72–74]. High pretreatment IVIM D and f values were also associated with the poor response of squamous cell cancer [75]. However, the predictive and prognostic value of ADC in this disease setting requires further validation.

24.4.3 Focal liver lesions

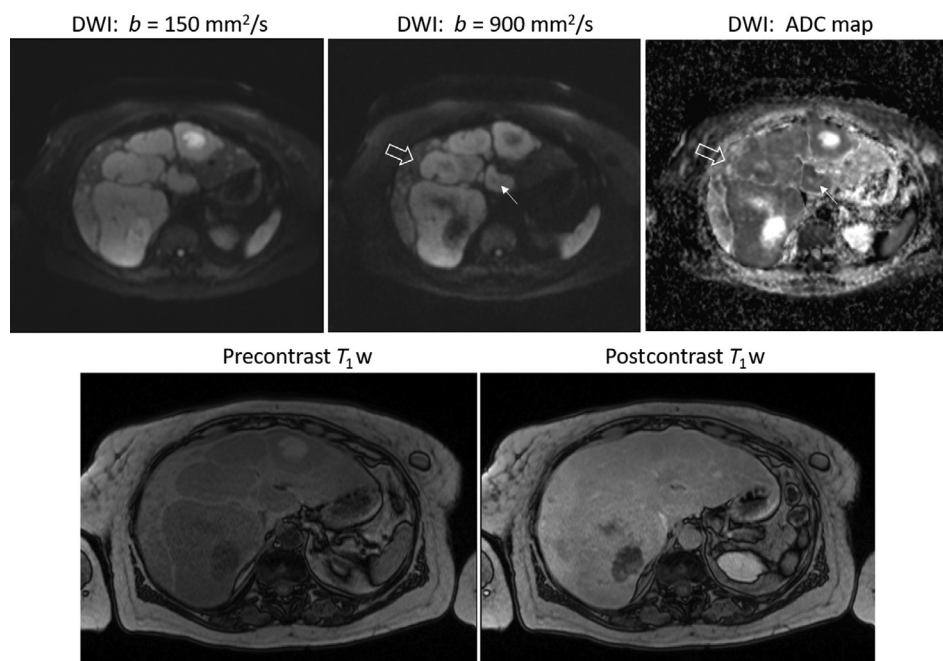
24.4.3.1 Disease detection and characterization

Diffusion imaging using b -values greater than $50\text{--}100 \text{ s/mm}^2$ suppresses the intrahepatic vascular signal, improving the detection of small focal liver lesions compared with T_2 or contrast-enhanced images, and also improves the reader confidence [75–77]. However, the combination of diffusion images with contrast-enhanced images is superior to either sequence by itself for the detection of colorectal liver metastases [75, 76] (Fig. 24.7). Diffusion imaging is deemed the most sensitive contrast for the detection of neuroendocrine liver metastases [78]. In the noncirrhotic liver, an ADC value greater than $1.7 \times 10^{-3} \text{ mm}^2/\text{s}$ has good diagnostic sensitivity and specificity for discrimination between benign and malignant focal lesions but should be combined with all morphological imaging findings and not used as a stand-alone criterion due to the considerable overlap of ADC values between benign and malignant lesions.

In the cirrhotic liver, lesion detection for hepatocellular carcinoma (HCC) is reduced as fibrosis leads to impeded diffusion of the parenchyma, thus reducing the lesion to parenchyma contrast [79]. An inverse correlation between ADC and tumor grade in HCC was shown in multiple studies. More recently, IVIM diffusion parameters performed better than conventional DWI for assessing tumor grade [80].

24.4.3.2 Response assessment

Diffusion imaging has shown promising results for assessing tumor response to interventional procedures and systemic therapies. ADC increase is associated with the degree of necrosis after transarterial chemoembolization (TACE) [81, 82]; observable blood flow reduction after transarterial radioembolization (TARE) may be assessed by IVIM f measurements [83], and high ADC values after radiation therapy are associated with a recurrence-free survival of HCC patients [84]. An increase in the ADC values of metastases was observed in response to systemic chemotherapy with responders

**FIG. 24.7**

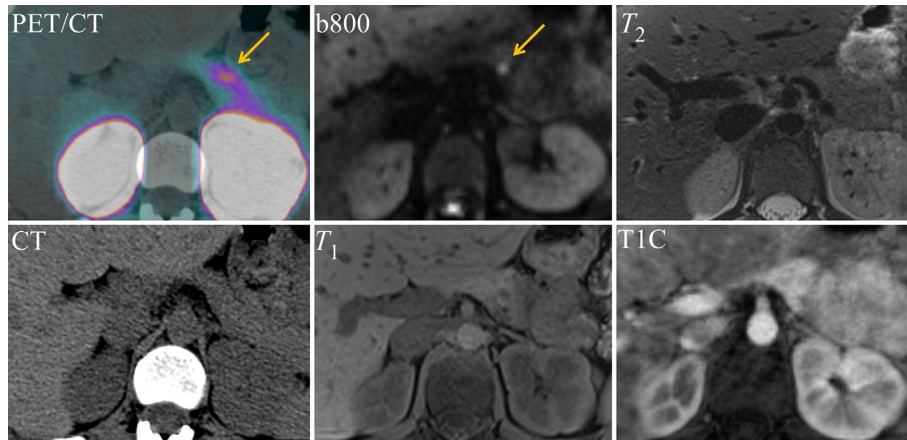
Liver metastasis of 66-year-old woman with known colorectal cancer. Intrahepatic cellular lesions, such as metastases, are easily identified on diffusion-weighted imaging (*arrows*). Diffusion-weighted images (top row) showing the lower ($b150$) and higher ($b900$) b -value images, as well as the corresponding ADC map. The smaller lesion at the hepatic hilum (*thin arrow*) returned an ADC value of $0.9 \times 10^{-3} \text{ mm}^2/\text{s}$, while normal liver ADC (right lobe) was $1.1 \times 10^{-3} \text{ mm}^2/\text{s}$. Pre/postcontrast T_1 -weighted images are also shown (bottom row) demonstrating lower lesion conspicuity compared with the diffusion-weighted images.

showing 26% ADC increase 7 days after treatment [25]. Moreover, ADC changes precede a reduction in the size of responding hepatic metastases [85]. However, the percentage of ADC increase that is associated with longer-term improved treatment outcomes requires validation.

24.4.4 Focal pancreatic lesions

24.4.4.1 Disease detection

The pancreas appears largely homogenous on diffusion images [86]. An inhomogeneous diffusion signal of the parenchyma should raise suspicion for disease. Using diffusion imaging can improve tumor detection compared with conventional T_2 -weighted images [87]. Very high detection rates and diagnostic accuracy of 96% have been reported for ductal adenocarcinomas, using a pooled mean ADC of less than $1.332 \times 10^{-3} \text{ mm}^2/\text{s}$ as a threshold for a suspicious focal abnormality [87, 88]. Besides, the pseudodiffusion fraction (f') measured in IVIM is decreased in adenocarcinomas and has shown superior diagnostic performance over ADC or D values [89, 90]. Diffusion imaging is even more sensitive and accurate for the detection of pancreatic neuroendocrine tumors (NETs) [88] (Fig. 24.8).

**FIG. 24.8**

Insulinoma in a 40-year-old patient. The *yellow arrows* point to a 0.5 cm tumor in the body of the pancreas with increased metabolic activity on the DOTATOC PET/CT, which is also easily seen on the b800 diffusion-weighted image. The lesion is however not visible on the CT, T_2 -weighted (T_2), T_1 -weighted (T_1) or post-contrast T_1 -weighted (T1C) images.

24.4.4.2 Characterization of malignancy

The mean ADC value of normal parenchyma ranges from $1.270\text{--}0.611 \times 10^{-3} \text{ mm}^2/\text{s}$ [86]. However, conflicting results have been published resulting in overlapping ADC ranges for mass-forming pancreatitis and adenocarcinoma [88]. The ADC value is inversely correlated with tumor grade in neuroendocrine tumors [91]. IVIM diffusion imaging is useful for characterizing pancreatic masses: f and D^* were significantly higher in neuroendocrine tumors than in adenocarcinoma (but lower than normal parenchyma), and showed superior diagnostic accuracy over other diffusion parameters for discrimination between the two malignant entities with the excellent interreader agreement [92–94].

24.4.5 Renal masses and renal function

24.4.5.1 Lesion detection and characterization

Diffusion imaging is routinely utilized in renal cancer imaging. A metaanalysis including 764 patients across 17 studies concluded that DWI can be used to discriminate between malignant and benign focal renal lesions [95]. Mean ADC values were significantly lower in renal cell carcinoma ($1.61 \times 10^{-3} \text{ mm}^2/\text{s}$) and uroepithelial malignancies ($1.30 \times 10^{-3} \text{ mm}^2/\text{s}$) than in normal parenchyma ($2.10 \times 10^{-3} \text{ mm}^2/\text{s}$) and oncocytomas ($2.00 \times 10^{-3} \text{ mm}^2/\text{s}$). In a further metaanalysis including 397 renal cell carcinomas (RCC), DWI showed moderate diagnostic performance for differentiating between high- and low-grade RCC [96]. However, it is again important to note that lesion characterization of renal tumors should not be entirely reliant on ADC due to the overlap of the ADC values between different pathologies, and should be interpreted alongside all other imaging findings.

24.4.5.2 Renal function

Early-stage kidney disease was found to be associated with lower ADC values than normal parenchyma, making diffusion mapping a potentially useful tool to monitor the function of the native or transplanted kidney (Fig. 24.9). ADC values showed a negative linear correlation with increasing grade of kidney disease [97]. The kidneys receive about 25% of the cardiac output volume. Conversely, this translates into strong cortical perfusion and medullary tubular flow, which affects ADC measurements. Thus, using IVIM diffusion imaging, the cortical IVIM parameters f , D , and D^* were significantly lower in patients with chronic kidney disease than in healthy individuals [98]. Besides, a negative correlation has been reported between f and D with 24-h urinary protein, serum creatine levels, and histopathological glomerular injury and fibrosis score. The f and D values showed a positive correlation with eGFR [98, 99].

24.4.6 Gynecological tumors

24.4.6.1 Endometrial cancer

The use of diffusion imaging increases the detection rate of endometrial cancer when added to T_2 -weighted images versus T_2 -weighted images alone, and is especially helpful where leiomyomas or adenomyosis cause altered anatomy [100]. Besides, diffusion imaging can aid disease staging by accurately assessing myometrial invasion. Diffusion measurements can help the physician to avoid the pitfall of including peri-tumoral inflammation, which has similar contrast enhancement compared to malignancy but which does not show impeded diffusion [101].

24.4.6.2 Cervical cancer

Diffusion imaging is as accurate as contrast-enhanced MRI for detecting cervical cancer (diagnostic accuracy=0.95) [102]. ADC values were shown to inversely correlate with tumor grade [103, 104]. Diffusion measurements can help to delineate small tumors for surgical planning [105]. Diffusion imaging is useful for following up chemoradiation treatment and can detect disease recurrence and monitor tumor response—a significant increase in ADC values has been reported in responders as early as 2 weeks after initiating therapy [106].

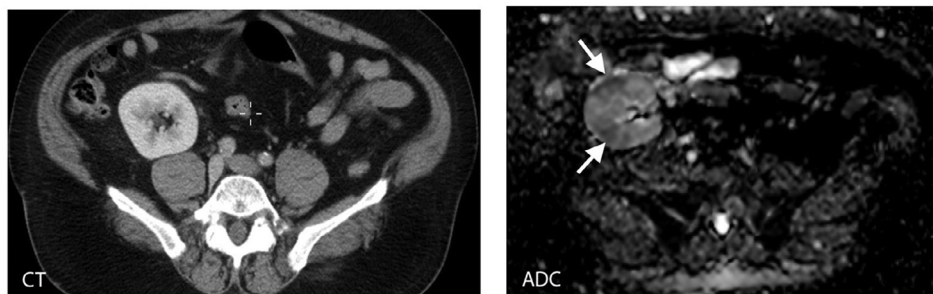


FIG. 24.9

A 54-year-old man with a transplant kidney in the right iliac fossa presenting with slight impairment of renal function. Axial contrast-enhanced CT in the portovenous phase shows differential enhancement of the cortex and medulla but no focal abnormality is detected. The MRI-derived ADC map shows focal areas of low ADC values in the renal parenchyma in keeping with focal nephritis.

24.4.6.3 Adnexal masses

Diffusion imaging has recently been included as a standard contrast for assessing sonographically indeterminate adnexal masses by the European Society of Urogenital Radiology [107]. Diffusion is included in the adnexal masses MRI scoring system and is deemed especially helpful when assessing nonlipomatous, nonhemorrhagic solid, or complex lesions [108]. Such adnexal masses with ADC values lower than $1.00 \times 10^{-3} \text{ mm}^2/\text{s}$ should be viewed with suspicion. Conversely, a low T_2 -signal mass associated with low signal intensity on DWI is highly predictive of benignity [103]. Diffusion imaging can also improve disease staging and surveillance by reliably identifying peritoneal deposits and recurrent disease [103].

24.4.7 Prostate cancer

The prostate is one of the most active areas of extracranial diffusion imaging research. In combination with T_2 -weighted MRI, DWI (together with the ADC map) has become one of the key sequences for tumor detection and staging. This approach is encapsulated in the Prostate Imaging Reporting and Data System (PIRADS). In the most recent version 2.1, DWI is termed the dominant sequence for assessing tumors of the peripheral zone [109]. For ADC calculation, a low b -value between 0–100 s/mm² and a high b -value less than 1000 s/mm² are recommended. The ADC value has been shown to inversely correlate with the Gleason score [110] and may indicate tumor progression on serial measurements [111] or tumor relapse following treatment [112]. PIRADS also recommends separate acquisition of an ultrahigh b -value (greater than 1400 s/mm²) [109], which may help with lesion detection and also discrimination between glandular hyperplasia and transition zone tumors [113]. In a metaanalysis of 789 patients across 11 studies, measurements with high b -values greater than 1000 s/mm² showed better diagnostic accuracy than standard high b -values between 800–1000 s/mm² for detecting prostate cancer (pooled sensitivity 80% versus 78% and specificity 92% versus 87%) [114]. A promising application for diffusion imaging in this context is computed high b -values. Computed b1500 and b2000 images showed higher diagnostic accuracy than acquired b1000 images and comparable performance to acquired ultrahigh b -value images [115, 116].

24.4.8 Bone marrow disease: Myeloma, bone metastases

Adult bone marrow represents a unique environment for diffusion imaging because of its high-fat content. The large fat cells paired with complex trabecular bone structure lead to a signal suppression on DWI and very low ADC values in healthy bone (vertebral bone ADC $0.2\text{--}0.5 \times 10^{-3} \text{ mm}^2/\text{s}$). The presence of bone marrow disease results in high signal on DWI but paradoxically higher ADC values (typically greater than $0.5 \times 10^{-3} \text{ mm}^2/\text{s}$). WB-DWI is superior to radionuclide bone scans, and at least equivalent if not superior to ¹⁸F-choline PET for the detection of bone metastases from prostate cancer [117]. WB-DWI has also been shown to be better than ¹⁸F-FDG PET for the detection of focal disease and diffuse disease in myeloma in all body parts except the skull [58]. DWI is also of value in discriminating between malignant and benign lesions such as hemangiomas [118]. Besides, tDV and gADC can be monitored during treatment and have shown promising results as biomarkers for therapy response and failure [53–56, 119]. Reporting and data systems for whole-body DWI, aiming to achieve standardization for imaging of advanced prostate cancer and multiple myeloma have been developed and published recently by multidisciplinary expert panels of radiologists, medical physicists, and clinicians [120, 121].

24.5 Future developments

Further developments in hardware and software will undoubtedly consolidate the role of extracranial diffusion imaging in clinical care. One of the disadvantages of MRI as a technique is the comparative long acquisition time compared with CT, especially for WB-DWI studies. Techniques that can improve acquisition efficiency, such as simultaneous multislice acquisitions (Fig. 24.10), or improve image reconstruction from sparse sampling will help to make the technique even more accessible within the radiological community.

Further developments of quantitative diffusion values as biomarkers will continue to evolve. Larger multicenter studies are underway to investigate and validate quantitative ADC values as a diagnostic, response, and prognostic biomarkers. Recent trials using WB-MRI including diffusion imaging in

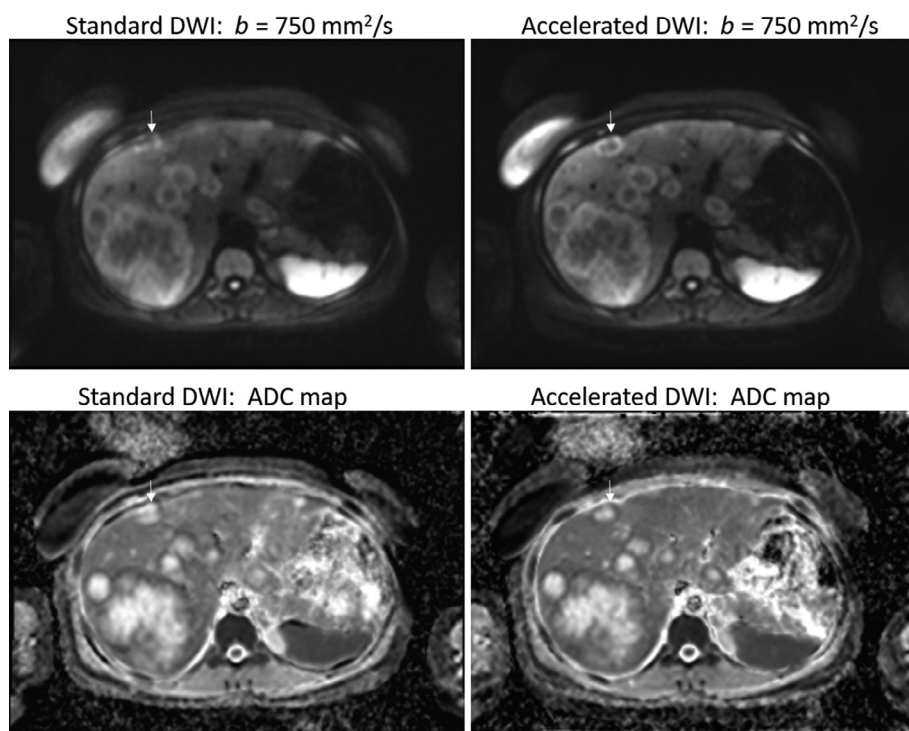


FIG. 24.10

A 53-year-old woman with colorectal liver metastases. Standard (left) versus accelerated (right) DWI demonstrating faster acquisition (3:37 versus 2:46 min) and improved quality (*white arrows*) using the accelerated protocol. Both DWIs were acquired under free-breathing using a monopolar scheme with 3 b -values (0, 100, 750), four signal averages per b -value, TE/TR = 53/7000 ms and a resolution of $1.5 \times 1.5 \times 6 \text{ mm}^3$. The accelerated DWI used a prototype sequence that allowed a slice acceleration factor of 2 and a reduced TR of 5000 ms while keeping the other parameters similar. The prototype sequence also employed a motion correction algorithm.

patients with newly diagnosed lung and colorectal cancer [122] have shown that diffusion imaging can potentially replace the conventional imaging pathways of using CT and PET-CT for disease staging. However, real-world implementation of the technique may be challenging and better radiological education and training in these areas are imperative. Last but not least, artificial intelligence and machine learning are major disruptors in radiology, which are advancing at a rapid pace. There is potential to harness these technologies across the whole spectrum from image acquisition, data modeling, and image interpretation to drive innovations in body diffusion imaging.

References

- [1] Hahn E. Spin echoes. *Phys Rev* 1950;80:580.
- [2] Stejskal E, Tanner J. Spin diffusion measurements: spin echoes in the presence of a time-dependent field gradient. *J Chem Phys* 1965;1(42):288–92.
- [3] Jaermann T, Pruessmann KP, Valavanis A, Kollias S, Boesiger P. Influence of SENSE on image properties in high-resolution single-shot echo-planar DTI. *Magn Reson Med* 2006;55(2):335–42. <https://doi.org/10.1002/mrm.20769>.
- [4] Jerome NP, Orton MR, d'Arcy JA, Collins DJ, Koh DM, Leach MO. Comparison of free-breathing with navigator-controlled acquisition regimes in abdominal diffusion-weighted magnetic resonance images: effect on ADC and IVIM statistics. *J Magn Reson Imaging* 2014;39(1):235–40. <https://doi.org/10.1002/jmri.24140>.
- [5] Koh DM, Blackledge M, Padhani AR, Takahara T, Kwee TC, Leach MO, Collins DJ. Whole-body diffusion-weighted MRI: tips, tricks, and pitfalls. *AJR Am J Roentgenol* 2012;199(2):252–62. <https://doi.org/10.2214/AJR.11.7866>.
- [6] Dietrich O, Biffar A, Baur-Melnyk A, Reiser MF. Technical aspects of MR diffusion imaging of the body. *Eur J Radiol* 2010;76(3):314–22. <https://doi.org/10.1016/j.ejrad.2010.02.018>.
- [7] Deng J, Omary RA, Larson AC. Multishot diffusion-weighted SPLICE PROPELLER MRI of the abdomen. *Magn Reson Med* 2008;59(5):947–53. <https://doi.org/10.1002/mrm.21525>.
- [8] Feinberg DA, Hoenninger JC, Crooks LE, Kaufman L, Watts JC, Arakawa M. Inner volume MR imaging: technical concepts and their application. *Radiology* 1985;156(3):743–7. <https://doi.org/10.1148/radiology.156.3.4023236>.
- [9] Wilm BJ, Svensson J, Henning A, Pruessmann KP, Boesiger P, Kollias SS. Reduced field-of-view MRI using outer volume suppression for spinal cord diffusion imaging. *Magn Reson Med* 2007;57(3):625–30. <https://doi.org/10.1002/mrm.21167>.
- [10] Kim H, Lee JM, Yoon JH, Jang JY, Kim SW, Ryu JK, Kannengiesser S, Han JK, Choi BI. Reduced field-of-view diffusion-weighted magnetic resonance imaging of the pancreas: comparison with conventional single-shot echo-planar imaging. *Korean J Radiol* 2015;16(6):1216–25. <https://doi.org/10.3348/kjr.2015.16.6.1216>.
- [11] Hwang J, Hong SS, Kim HJ, Chang YW, Nam BD, Oh E, Lee E, Cha H. Reduced field-of-view diffusion-weighted MRI in patients with cervical cancer. *Br J Radiol* 2018;91(1087):20170864. <https://doi.org/10.1259/bjr.20170864>.
- [12] Vidiri A, Minosse S, Piludu F, Curione D, Pichi B, Spriano G, Marzi S. Feasibility study of reduced field of view diffusion-weighted magnetic resonance imaging in head and neck tumors. *Acta Radiol* 2017; 58(3):292–300. <https://doi.org/10.1177/0284185116652014>.
- [13] Warndahl BA, Borisch EA, Kawashima A, Riederer SJ, Froemming AT. Conventional vs. reduced field of view diffusion weighted imaging of the prostate: comparison of image quality, correlation with histology, and inter-reader agreement. *Magn Reson Imaging* 2018;47:67–76. <https://doi.org/10.1016/j.mri.2017.10.011>.
- [14] Porter DA, Heidemann RM. High resolution diffusion-weighted imaging using readout-segmented echo-planar imaging, parallel imaging and a two-dimensional navigator-based reacquisition. *Magn Reson Med* 2009;62(2):468–75. <https://doi.org/10.1002/mrm.22024>.

- [15] Blackledge MD, Leach MO, Collins DJ, Koh DM. Computed diffusion-weighted MR imaging may improve tumor detection. *Radiology* 2011;261(2):573–81. <https://doi.org/10.1148/radiol.11101919>.
- [16] O'Flynn EA, Blackledge M, Collins D, Downey K, Doran S, Patel H, Dumonteil S, Mok W, Leach MO, Koh DM. Evaluating the diagnostic sensitivity of computed diffusion-weighted MR imaging in the detection of breast cancer. *J Magn Reson Imaging* 2016;44(1):130–7. <https://doi.org/10.1002/jmri.25131>.
- [17] Soher BJ, Dale BM, Merkle EM. A review of MR physics: 3T versus 1.5T. *Magn Reson Imaging Clin N Am* 2007;15(3):277–90. <https://doi.org/10.1016/j.mric.2007.06.002>.
- [18] Lavdas I, Miquel ME, McRobbie DW, Aboagye EO. Comparison between diffusion-weighted MRI (DW-MRI) at 1.5 and 3 tesla: a phantom study. *J Magn Reson Imaging* 2014;40(3):682–90. <https://doi.org/10.1002/jmri.24397>.
- [19] Rosenkrantz AB, Oei M, Babb JS, Niver BE, Taouli B. Diffusion-weighted imaging of the abdomen at 3.0 tesla: image quality and apparent diffusion coefficient reproducibility compared with 1.5 tesla. *J Magn Reson Imaging* 2011;33(1):128–35. <https://doi.org/10.1002/jmri.22395>.
- [20] Beyersdorff D, Taymoorian K, Knösel T, Schnorr D, Felix R, Hamm B, Bruhn H. MRI of prostate cancer at 1.5 and 3.0 T: comparison of image quality in tumor detection and staging. *AJR Am J Roentgenol* 2005;185(5):1214–20. <https://doi.org/10.2214/AJR.04.1584>.
- [21] Matsuoka A, Minato M, Harada M, Kubo H, Bandou Y, Tangoku A, Nakano K, Nishitani H. Comparison of 3.0- and 1.5-tesla diffusion-weighted imaging in the visibility of breast cancer. *Radiat Med* 2008;26(1):15–20. <https://doi.org/10.1007/s11604-007-0187-6>.
- [22] Zhang H, Xue H, Alto S, Hui L, Kannengiesser S, Berthold K, Jin Z. Integrated shimming improves lesion detection in whole-body diffusion-weighted examinations of patients with plasma disorder at 3 T. *Investig Radiol* 2016;51(5):297–305. <https://doi.org/10.1097/RLI.0000000000000238>.
- [23] Donners R, Blackledge M, Tunariu N, Messiou C, Merkle EM, Koh DM. Quantitative whole-body diffusion-weighted MR imaging. *Magn Reson Imaging Clin N Am* 2018;26(4):479–94. <https://doi.org/10.1016/j.mric.2018.06.002>.
- [24] Sun Y, Tong T, Cai S, Bi R, Xin C, Gu Y. Apparent diffusion coefficient (ADC) value: a potential imaging biomarker that reflects the biological features of rectal cancer. *PLoS One* 2014;9(10):e109371. <https://doi.org/10.1371/journal.pone.0109371>.
- [25] Cui Y, Zhang XP, Sun YS, Tang L, Shen L. Apparent diffusion coefficient: potential imaging biomarker for prediction and early detection of response to chemotherapy in hepatic metastases. *Radiology* 2008;248(3):894–900. <https://doi.org/10.1148/radiol.2483071407>.
- [26] Lambrecht M, Van Calster B, Vandecaveye V, De Keyzer F, Roebben I, Hermans R, Nuyts S. Integrating pretreatment diffusion weighted MRI into a multivariable prognostic model for head and neck squamous cell carcinoma. *Radiother Oncol* 2014;110(3):429–34. <https://doi.org/10.1016/j.radonc.2014.01.004>.
- [27] Donati OF, Chong D, Nanz D, Boss A, Froehlich JM, Andres E, Seifert B, Thoeny HC. Diffusion-weighted MR imaging of upper abdominal organs: field strength and intervender variability of apparent diffusion coefficients. *Radiology* 2014;270(2):454–63. <https://doi.org/10.1148/radiol.13130819>.
- [28] Moreau B, Iannessi A, Hoog C, Beaumont H. How reliable are ADC measurements? A phantom and clinical study of cervical lymph nodes. *Eur Radiol* 2018. <https://doi.org/10.1007/s00330-017-5265-2>.
- [29] Sadinski M, Medved M, Karademir I, Wang S, Peng Y, Jiang Y, Sammet S, Karczmar G, Oto A. Short-term reproducibility of apparent diffusion coefficient estimated from diffusion-weighted MRI of the prostate. *Abdom Imaging* 2015;40(7):2523–8. <https://doi.org/10.1007/s00261-015-0396-x>.
- [30] Braithwaite AC, Dale BM, Boll DT, Merkle EM. Short- and midterm reproducibility of apparent diffusion coefficient measurements at 3.0-T diffusion-weighted imaging of the abdomen. *Radiology* 2009;250(2):459–65. <https://doi.org/10.1148/radiol.2502080849>.
- [31] Sasaki M, Yamada K, Watanabe Y, Matsui M, Ida M, Fujiwara S, Shibata E, Investigators ASISG-JA-J. Variability in absolute apparent diffusion coefficient values across different platforms may be substantial: a multivendor, multi-institutional comparison study. *Radiology* 2008;249(2):624–30. <https://doi.org/10.1148/radiol.2492071681>.

- [32] Jerome NP, Miyazaki K, Collins DJ, Orton MR, d'Arcy JA, Wallace T, Moreno L, Pearson AD, Marshall LV, Carceller F, Leach MO, Zacharoulis S, Koh DM. Repeatability of derived parameters from histograms following non-Gaussian diffusion modelling of diffusion-weighted imaging in a paediatric oncological cohort. *Eur Radiol* 2017;27(1):345–53. <https://doi.org/10.1007/s00330-016-4318-2>.
- [33] De Paepe KN, De Keyzer F, Wolter P, Bechter O, Dierickx D, Janssens A, Verhoef G, Oyen R, Vandecaveye V. Improving lymph node characterization in staging malignant lymphoma using first-order ADC texture analysis from whole-body diffusion-weighted MRI. *J Magn Reson Imaging* 2018. <https://doi.org/10.1002/jmri.26034>.
- [34] Blackledge MD, Tunariu N, Orton MR, Padhani AR, Collins DJ, Leach MO, Koh DM. Inter- and intra-observer repeatability of quantitative whole-body, diffusion-weighted imaging (WBDWI) in metastatic bone disease. *PLoS One* 2016;11(4):e0153840. <https://doi.org/10.1371/journal.pone.0153840>.
- [35] Winfield JM, Tunariu N, Rata M, Miyazaki K, Jerome NP, Germuska M, Blackledge MD, Collins DJ, de Bono JS, Yap TA, de Souza NM, Doran SJ, Koh DM, Leach MO, Messiou C, Orton MR. Extracranial soft-tissue tumors: repeatability of apparent diffusion coefficient estimates from diffusion-weighted MR imaging. *Radiology* 2017;284(1):88–99. <https://doi.org/10.1148/radiol.2017161965>.
- [36] Le Bihan D, Breton E, Lallemand D, Grenier P, Cabanis E, Laval-Jeantet M. MR imaging of intravoxel incoherent motions: application to diffusion and perfusion in neurologic disorders. *Radiology* 1986;161(2):401–7. <https://doi.org/10.1148/radiology.161.2.3763909>.
- [37] Koh DM, Collins DJ, Orton MR. Intravoxel incoherent motion in body diffusion-weighted MRI: reality and challenges. *AJR Am J Roentgenol* 2011;196(6):1351–61. <https://doi.org/10.2214/AJR.10.5515>.
- [38] Jerome NP, d'Arcy JA, Feiweier T, Koh DM, Leach MO, Collins DJ, Orton MR. Extended T2-IVIM model for correction of TE dependence of pseudo-diffusion volume fraction in clinical diffusion-weighted magnetic resonance imaging. *Phys Med Biol* 2016;61(24):N667–80. <https://doi.org/10.1088/1361-6560/61/24/N667>.
- [39] Andreou A, Koh DM, Collins DJ, Blackledge M, Wallace T, Leach MO, Orton MR. Measurement reproducibility of perfusion fraction and pseudodiffusion coefficient derived by intravoxel incoherent motion diffusion-weighted MR imaging in normal liver and metastases. *Eur Radiol* 2013;23(2):428–34. <https://doi.org/10.1007/s00330-012-2604-1>.
- [40] Dyvorne H, Jajamovich G, Kakite S, Kuehn B, Taouli B. Intravoxel incoherent motion diffusion imaging of the liver: optimal b-value subsampling and impact on parameter precision and reproducibility. *Eur J Radiol* 2014;83(12):2109–13. <https://doi.org/10.1016/j.ejrad.2014.09.003>.
- [41] Klauss M, Lemke A, Grünberg K, Simon D, Re TJ, Wente MN, Laun FB, Kauczor HU, Delorme S, Grenacher L, Stieltjes B. Intravoxel incoherent motion MRI for the differentiation between mass forming chronic pancreatitis and pancreatic carcinoma. *Investig Radiol* 2011;46(1):57–63. <https://doi.org/10.1097/RLI.0b013e3181fb3bf2>.
- [42] Chandarana H, Kang SK, Wong S, Rusinek H, Zhang JL, Arizono S, Huang WC, Melamed J, Babb JS, Suan EF, Lee VS, Sigmund EE. Diffusion-weighted intravoxel incoherent motion imaging of renal tumors with histopathologic correlation. *Investig Radiol* 2012;47(12):688–96. <https://doi.org/10.1097/RLI.0b013e31826a0a49>.
- [43] Fujima N, Yoshida D, Sakashita T, Homma A, Tsukahara A, Tha KK, Kudo K, Shirato H. Intravoxel incoherent motion diffusion-weighted imaging in head and neck squamous cell carcinoma: assessment of perfusion-related parameters compared to dynamic contrast-enhanced MRI. *Magn Reson Imaging* 2014;32(10):1206–13. <https://doi.org/10.1016/j.mri.2014.08.009>.
- [44] Suo S, Lin N, Wang H, Zhang L, Wang R, Zhang S, Hua J, Xu J. Intravoxel incoherent motion diffusion-weighted MR imaging of breast cancer at 3.0 tesla: comparison of different curve-fitting methods. *J Magn Reson Imaging* 2015;42(2):362–70. <https://doi.org/10.1002/jmri.24799>.
- [45] Iima M, Le Bihan D. Clinical intravoxel incoherent motion and diffusion MR imaging: past, present, and future. *Radiology* 2016;278(1):13–32. <https://doi.org/10.1148/radiol.2015150244>.

- [46] Wang Y, Hu D, Yu H, Shen Y, Tang H, Kamel IR, Li Z. Comparison of the diagnostic value of monoexponential, biexponential, and stretched exponential diffusion-weighted MRI in differentiating tumor stage and histological grade of bladder cancer. *Acad Radiol* 2019;26(2):239–46. <https://doi.org/10.1016/j.acra.2018.04.016>.
- [47] Bennett KM, Schmainda KM, Bennett RT, Rowe DB, Lu H, Hyde JS. Characterization of continuously distributed cortical water diffusion rates with a stretched-exponential model. *Magn Reson Med* 2003;50(4):727–34. <https://doi.org/10.1002/mrm.10581>.
- [48] Anderson SW, Barry B, Soto J, Ozonoff A, O'Brien M, Jara H. Characterizing non-Gaussian, high b-value diffusion in liver fibrosis: stretched exponential and diffusional kurtosis modeling. *J Magn Reson Imaging* 2014;39(4):827–34. <https://doi.org/10.1002/jmri.24234>.
- [49] Jin YN, Zhang Y, Cheng JL, Zheng DD, Hu Y. Monoexponential, biexponential, and stretched-exponential models using diffusion-weighted imaging: a quantitative differentiation of breast lesions at 3T. *J Magn Reson Imaging* 2019. <https://doi.org/10.1002/jmri.26729>.
- [50] Fujima N, Yoshida D, Sakashita T, Homma A, Kudo K, Shirato H. Residual tumour detection in post-treatment granulation tissue by using advanced diffusion models in head and neck squamous cell carcinoma patients. *Eur J Radiol* 2017;90:14–9. <https://doi.org/10.1016/j.ejrad.2017.02.025>.
- [51] Winfield JM, de Souza NM, Priest AN, Wakefield JC, Hodgkin C, Freeman S, Orton MR, Collins DJ. Modeling DW-MRI data from primary and metastatic ovarian tumours. *Eur Radiol* 2015;25(7):2033–40. <https://doi.org/10.1007/s00330-014-3573-3>.
- [52] Takahara T, Imai Y, Yamashita T, Yasuda S, Nasu S, Van Cauteren M. Diffusion weighted whole body imaging with background body signal suppression (DWIBS): technical improvement using free breathing, STIR and high resolution 3D display. *Radiat Med* 2004;22(4):275–82.
- [53] Blackledge MD, Collins DJ, Tunariu N, Orton MR, Padhani AR, Leach MO, Koh DM. Assessment of treatment response by total tumor volume and global apparent diffusion coefficient using diffusion-weighted MRI in patients with metastatic bone disease: a feasibility study. *PLoS One* 2014;9(4):e91779. <https://doi.org/10.1371/journal.pone.0091779>.
- [54] Perez-Lopez R, Lorente D, Blackledge MD, Collins DJ, Mateo J, Bianchini D, Omlin A, Zivi A, Leach MO, de Bono JS, Koh DM, Tunariu N. Volume of bone metastasis assessed with whole-body diffusion-weighted imaging is associated with overall survival in metastatic castration-resistant prostate cancer. *Radiology* 2016;280(1):151–60. <https://doi.org/10.1148/radiol.2015150799>.
- [55] Perez-Lopez R, Mateo J, Mossop H, Blackledge MD, Collins DJ, Rata M, Morgan VA, Macdonald A, Sandhu S, Lorente D, Rescigno P, Zafeiriou Z, Bianchini D, Porta N, Hall E, Leach MO, de Bono JS, Koh DM, Tunariu N. Diffusion-weighted imaging as a treatment response biomarker for evaluating bone metastases in prostate cancer: a pilot study. *Radiology* 2017;283(1):168–77. <https://doi.org/10.1148/radiol.2016160646>.
- [56] Giles SL, Messiou C, Collins DJ, Morgan VA, Simpkin CJ, West S, Davies FE, Morgan GJ, de Souza NM. Whole-body diffusion-weighted MR imaging for assessment of treatment response in myeloma. *Radiology* 2014;271(3):785–94. <https://doi.org/10.1148/radiol.13131529>.
- [57] Sinha S, Lucas-Quesada FA, Sinha U, DeBruhl N, Bassett LW. In vivo diffusion-weighted MRI of the breast: potential for lesion characterization. *J Magn Reson Imaging* 2002;15(6):693–704. <https://doi.org/10.1002/jmri.10116>.
- [58] Chen X, Li WL, Zhang YL, Wu Q, Guo YM, Bai ZL. Meta-analysis of quantitative diffusion-weighted MR imaging in the differential diagnosis of breast lesions. *BMC Cancer* 2010;10:693. <https://doi.org/10.1186/1471-2407-10-693>.
- [59] Zhang L, Tang M, Min Z, Lu J, Lei X, Zhang X. Accuracy of combined dynamic contrast-enhanced magnetic resonance imaging and diffusion-weighted imaging for breast cancer detection: a meta-analysis. *Acta Radiol* 2016;57(6):651–60. <https://doi.org/10.1177/0284185115597265>.
- [60] Bickelhaupt S, Laun FB, Tesdorff J, Lederer W, Daniel H, Stieber A, Delorme S, Schlemmer HP. Fast and noninvasive characterization of suspicious lesions detected at breast cancer X-ray screening: capability of diffusion-weighted MR imaging with MIPs. *Radiology* 2016;278(3):689–97. <https://doi.org/10.1148/radiol.2015150425>.

- [61] Peters NH, Vincken KL, van den Bosch MA, Luijten PR, Mali WP, Bartels LW. Quantitative diffusion weighted imaging for differentiation of benign and malignant breast lesions: the influence of the choice of b-values. *J Magn Reson Imaging* 2010;31(5):1100–5. <https://doi.org/10.1002/jmri.22152>.
- [62] Dorrius MD, Dijkstra H, Oudkerk M, Sijens PE. Effect of b value and pre-admission of contrast on diagnostic accuracy of 1.5-T breast DWI: a systematic review and meta-analysis. *Eur Radiol* 2014;24(11):2835–47. <https://doi.org/10.1007/s00330-014-3338-z>.
- [63] Costantini M, Belli P, Rinaldi P, Bufi E, Giardina G, Franceschini G, Petrone G, Bonomo L. Diffusion-weighted imaging in breast cancer: relationship between apparent diffusion coefficient and tumour aggressiveness. *Clin Radiol* 2010;65(12):1005–12. <https://doi.org/10.1016/j.crad.2010.07.008>.
- [64] Partridge SC, Nissan N, Rahbar H, Kitsch AE, Sigmund EE. Diffusion-weighted breast MRI: clinical applications and emerging techniques. *J Magn Reson Imaging* 2017;45(2):337–55. <https://doi.org/10.1002/jmri.25479>.
- [65] Choi SY, Chang YW, Park HJ, Kim HJ, Hong SS, Seo DY. Correlation of the apparent diffusion coefficient values on diffusion-weighted imaging with prognostic factors for breast cancer. *Br J Radiol* 2012;85(1016):e474–9. <https://doi.org/10.1259/bjr/79381464>.
- [66] Mori N, Ota H, Mugikura S, Takasawa C, Ishida T, Watanabe G, Tada H, Watanabe M, Takase K, Takahashi S. Luminal-type breast cancer: correlation of apparent diffusion coefficients with the Ki-67 labeling index. *Radiology* 2015;274(1):66–73. <https://doi.org/10.1148/radiol.14140283>.
- [67] Bickel H, Pinker-Domenig K, Bogner W, Spick C, Bagó-Horváth Z, Weber M, Helbich T, Baltzer P. Quantitative apparent diffusion coefficient as a noninvasive imaging biomarker for the differentiation of invasive breast cancer and ductal carcinoma in situ. *Investig Radiol* 2015;50(2):95–100. <https://doi.org/10.1097/RLI.0000000000000104>.
- [68] Wang J, Takashima S, Takayama F, Kawakami S, Saito A, Matsushita T, Momose M, Ishiyama T. Head and neck lesions: characterization with diffusion-weighted echo-planar MR imaging. *Radiology* 2001;220(3):621–30. <https://doi.org/10.1148/radiol.2202010063>.
- [69] Razek AA, Elkhamary S, Mousa A. Differentiation between benign and malignant orbital tumors at 3-T diffusion MR-imaging. *Neuroradiology* 2011;53(7):517–22. <https://doi.org/10.1007/s00234-011-0838-2>.
- [70] Srinivasan A, Dvorak R, Perni K, Rohrer S, Mukherji SK. Differentiation of benign and malignant pathology in the head and neck using 3T apparent diffusion coefficient values: early experience. *AJNR Am J Neuroradiol* 2008;29(1):40–4. <https://doi.org/10.3174/ajnr.A0743>.
- [71] King AD, Mo FK, Yu KH, Yeung DK, Zhou H, Bhatia KS, Tse GM, Vlantis AC, Wong JK, Ahuja AT. Squamous cell carcinoma of the head and neck: diffusion-weighted MR imaging for prediction and monitoring of treatment response. *Eur Radiol* 2010;20(9):2213–20. <https://doi.org/10.1007/s00330-010-1769-8>.
- [72] Kim S, Loevner L, Quon H, Sherman E, Weinstein G, Kilger A, Poptani H. Diffusion-weighted magnetic resonance imaging for predicting and detecting early response to chemoradiation therapy of squamous cell carcinomas of the head and neck. *Clin Cancer Res* 2009;15(3):986–94. <https://doi.org/10.1158/1078-0432.CCR-08-1287>.
- [73] Vandecaveye V, Dirix P, de Keyser F, de Beeck KO, Vander Poorten V, Roebben I, Nuyts S, Hermans R. Predictive value of diffusion-weighted magnetic resonance imaging during chemoradiotherapy for head and neck squamous cell carcinoma. *Eur Radiol* 2010;20(7):1703–14. <https://doi.org/10.1007/s00330-010-1734-6>.
- [74] Vaid S, Chandorkar A, Atre A, Shah D, Vaid N. Differentiating recurrent tumours from post-treatment changes in head and neck cancers: does diffusion-weighted MRI solve the eternal dilemma? *Clin Radiol* 2017;72(1):74–83. <https://doi.org/10.1016/j.crad.2016.09.019>.
- [75] Koh DM, Brown G, Riddell AM, Scurr E, Collins DJ, Allen SD, Chau I, Cunningham D, de Souza NM, Leach MO, Husband JE. Detection of colorectal hepatic metastases using MnDPDP MR imaging and diffusion-weighted imaging (DWI) alone and in combination. *Eur Radiol* 2008;18(5):903–10. <https://doi.org/10.1007/s00330-007-0847-z>.

- [76] Donati OF, Fischer MA, Chuck N, Hunziker R, Weishaupt D, Reiner CS. Accuracy and confidence of Gd-EOB-DTPA enhanced MRI and diffusion-weighted imaging alone and in combination for the diagnosis of liver metastases. *Eur J Radiol* 2013;82(5):822–8. <https://doi.org/10.1016/j.ejrad.2012.12.005>.
- [77] Vilgrain V, Esvan M, Ronot M, Caumont-Prim A, Aubé C, Chatellier G. A meta-analysis of diffusion-weighted and gadoxetic acid-enhanced MR imaging for the detection of liver metastases. *Eur Radiol* 2016;26(12):4595–615. <https://doi.org/10.1007/s00330-016-4250-5>.
- [78] d'Assignies G, Fina P, Bruno O, Vullierme MP, Tubach F, Paradis V, Sauvanet A, Ruszniewski P, Vilgrain V. High sensitivity of diffusion-weighted MR imaging for the detection of liver metastases from neuroendocrine tumors: comparison with T2-weighted and dynamic gadolinium-enhanced MR imaging. *Radiology* 2013;268(2):390–9. <https://doi.org/10.1148/radiol.13121628>.
- [79] Taouli B, Koh DM. Diffusion-weighted MR imaging of the liver. *Radiology* 2010;254(1):47–66. <https://doi.org/10.1148/radiol.09090021>.
- [80] Zhu SC, Liu YH, Wei Y, Li LL, Dou SW, Sun TY, Shi DP. Intravoxel incoherent motion diffusion-weighted magnetic resonance imaging for predicting histological grade of hepatocellular carcinoma: comparison with conventional diffusion-weighted imaging. *World J Gastroenterol* 2018;24(8):929–40. <https://doi.org/10.3748/wjg.v24.i8.929>.
- [81] Kamel IR, Bluemke DA, Eng J, Liapi E, Messersmith W, Reyes DK, Geschwind JF. The role of functional MR imaging in the assessment of tumor response after chemoembolization in patients with hepatocellular carcinoma. *J Vasc Interv Radiol* 2006;17(3):505–12. <https://doi.org/10.1097/01.RVI.0000200052.02183.92>.
- [82] Kamel IR, Liapi E, Reyes DK, Zahurak M, Bluemke DA, Geschwind JF. Unresectable hepatocellular carcinoma: serial early vascular and cellular changes after transarterial chemoembolization as detected with MR imaging. *Radiology* 2009;250(2):466–73. <https://doi.org/10.1148/radiol.2502072222>.
- [83] Pieper CC, Willinek WA, Meyer C, Ahmadzadehfah H, Kukuk GM, Sprinkart AM, Block W, Schild HH, Mürtz P. Intravoxel incoherent motion diffusion-weighted MR imaging for prediction of early arterial blood flow stasis in radioembolization of breast cancer liver metastases. *J Vasc Interv Radiol* 2016;27(9):1320–8. <https://doi.org/10.1016/j.jvir.2016.04.018>.
- [84] Yu JI, Park HC, Lim DH, Choi Y, Jung SH, Paik SW, Kim SH, Jeong WK, Kim YK. The role of diffusion-weighted magnetic resonance imaging in the treatment response evaluation of hepatocellular carcinoma patients treated with radiation therapy. *Int J Radiat Oncol Biol Phys* 2014;89(4):814–21. <https://doi.org/10.1016/j.ijrobp.2014.03.020>.
- [85] Koh DM, Scurr E, Collins D, Kanber B, Norman A, Leach MO, Husband JE. Predicting response of colorectal hepatic metastasis: value of pretreatment apparent diffusion coefficients. *AJR Am J Roentgenol* 2007;188(4):1001–8. <https://doi.org/10.2214/AJR.06.0601>.
- [86] Dale BM, Braithwaite AC, Boll DT, Merkle EM. Field strength and diffusion encoding technique affect the apparent diffusion coefficient measurements in diffusion-weighted imaging of the abdomen. *Investig Radiol* 2010;45(2):104–8. <https://doi.org/10.1097/RLI.0b013e3181c8ceac>.
- [87] Kartalis N, Lindholm TL, Aspelin P, Permert J, Albiin N. Diffusion-weighted magnetic resonance imaging of pancreas tumours. *Eur Radiol* 2009;19(8):1981–90. <https://doi.org/10.1007/s00330-009-1384-8>.
- [88] Barral M, Taouli B, Guiu B, Koh DM, Luciani A, Manfredi R, Vilgrain V, Hoeffel C, Kanematsu M, Soyer P. Diffusion-weighted MR imaging of the pancreas: current status and recommendations. *Radiology* 2015;274(1):45–63. <https://doi.org/10.1148/radiol.14130778>.
- [89] Concia M, Sprinkart AM, Penner AH, Brossart P, Gieseke J, Schild HH, Willinek WA, Mürtz P. Diffusion-weighted magnetic resonance imaging of the pancreas: diagnostic benefit from an intravoxel incoherent motion model-based 3 b-value analysis. *Investig Radiol* 2014;49(2):93–100. <https://doi.org/10.1097/RLI.0b013e3182a71cc3>.
- [90] Re TJ, Lemke A, Klauss M, Laun FB, Simon D, Grünberg K, Delorme S, Grenacher L, Manfredi R, Mucelli RP, Stieltjes B. Enhancing pancreatic adenocarcinoma delineation in diffusion derived intravoxel incoherent motion f-maps through automatic vessel and duct segmentation. *Magn Reson Med* 2011;66(5):1327–32. <https://doi.org/10.1002/mrm.22931>.

- [91] Wang Y, Chen ZE, Yaghami V, Nikolaidis P, McCarthy RJ, Merrick L, Miller FH. Diffusion-weighted MR imaging in pancreatic endocrine tumors correlated with histopathologic characteristics. *J Magn Reson Imaging* 2011;33(5):1071–9. <https://doi.org/10.1002/jmri.22541>.
- [92] Kang KM, Lee JM, Yoon JH, Kiefer B, Han JK, Choi BI. Intravoxel incoherent motion diffusion-weighted MR imaging for characterization of focal pancreatic lesions. *Radiology* 2014;270(2):444–53. <https://doi.org/10.1148/radiol.13122712>.
- [93] De Robertis R, Cardobi N, Ortolani S, Tinazzi Martini P, Stemmer A, Grimm R, Gobbo S, Butturini G, D’Onofrio M. Intravoxel incoherent motion diffusion-weighted MR imaging of solid pancreatic masses: reliability and usefulness for characterization. *Abdom Radiol (NY)* 2019;44(1):131–9. <https://doi.org/10.1007/s00261-018-1684-z>.
- [94] Kim B, Lee SS, Sung YS, Cheong H, Byun JH, Kim HJ, Kim JH. Intravoxel incoherent motion diffusion-weighted imaging of the pancreas: characterization of benign and malignant pancreatic pathologies. *J Magn Reson Imaging* 2017;45(1):260–9. <https://doi.org/10.1002/jmri.25334>.
- [95] Lassel EA, Rao R, Schwenke C, Schoenberg SO, Michaely HJ. Diffusion-weighted imaging of focal renal lesions: a meta-analysis. *Eur Radiol* 2014;24(1):241–9. <https://doi.org/10.1007/s00330-013-3004-x>.
- [96] Woo S, Suh CH, Kim SY, Cho JY, Kim SH. Diagnostic performance of DWI for differentiating high-from low-grade clear cell renal cell carcinoma: a systematic review and meta-analysis. *AJR Am J Roentgenol* 2017;209(6):W374–81. <https://doi.org/10.2214/AJR.17.18283>.
- [97] Liu H, Zhou Z, Li X, Li C, Wang R, Zhang Y, Niu G. Diffusion-weighted imaging for staging chronic kidney disease: a meta-analysis. *Br J Radiol* 2018;91(1091):20170952. <https://doi.org/10.1259/bjr.20170952>.
- [98] Mao W, Zhou J, Zeng M, Ding Y, Qu L, Chen C, Ding X, Wang Y, Fu C. Chronic kidney disease: pathological and functional evaluation with intravoxel incoherent motion diffusion-weighted imaging. *J Magn Reson Imaging* 2018;47(5):1251–9. <https://doi.org/10.1002/jmri.25861>.
- [99] Mao W, Zhou J, Zeng M, Ding Y, Qu L, Chen C, Ding X, Wang Y, Fu C, Gu F. Intravoxel incoherent motion diffusion-weighted imaging for the assessment of renal fibrosis of chronic kidney disease: a preliminary study. *Magn Reson Imaging* 2018;47:118–24. <https://doi.org/10.1016/j.mri.2017.12.010>.
- [100] Inada Y, Matsuki M, Nakai G, Tatsugami F, Tanikake M, Narabayashi I, Yamada T, Tsuji M. Body diffusion-weighted MR imaging of uterine endometrial cancer: is it helpful in the detection of cancer in nonenhanced MR imaging? *Eur J Radiol* 2009;70(1):122–7. <https://doi.org/10.1016/j.ejrad.2007.11.042>.
- [101] Sala E, Rockall A, Rangarajan D, Kubik-Huch RA. The role of dynamic contrast-enhanced and diffusion weighted magnetic resonance imaging in the female pelvis. *Eur J Radiol* 2010;76(3):367–85. <https://doi.org/10.1016/j.ejrad.2010.01.026>.
- [102] Kuang F, Yan Z, Li H, Feng H. Diagnostic accuracy of diffusion-weighted MRI for differentiation of cervical cancer and benign cervical lesions at 3T: comparison with routine MRI and dynamic contrast-enhanced MRI. *J Magn Reson Imaging* 2015;42(4):1094–9. <https://doi.org/10.1002/jmri.24894>.
- [103] Addley H, Moyle P, Freeman S. Diffusion-weighted imaging in gynaecological malignancy. *Clin Radiol* 2017;72(11):981–90. <https://doi.org/10.1016/j.crad.2017.07.014>.
- [104] Xue H, Ren C, Yang J, Sun Z, Li S, Jin Z, Shen K, Zhou W. Histogram analysis of apparent diffusion coefficient for the assessment of local aggressiveness of cervical cancer. *Arch Gynecol Obstet* 2014;290(2):341–8. <https://doi.org/10.1007/s00404-014-3221-9>.
- [105] Nougaret S, Tirumani SH, Addley H, Pandey H, Sala E, Reinhold C. Pearls and pitfalls in MRI of gynecologic malignancy with diffusion-weighted technique. *AJR Am J Roentgenol* 2013;200(2):261–76. <https://doi.org/10.2214/AJR.12.9713>.
- [106] Harry VN, Semple SI, Gilbert FJ, Parkin DE. Diffusion-weighted magnetic resonance imaging in the early detection of response to chemoradiation in cervical cancer. *Gynecol Oncol* 2008;111(2):213–20. <https://doi.org/10.1016/j.ygyno.2008.07.048>.
- [107] Forstner R, Thomassin-Naggara I, Cunha TM, Kinkel K, Masselli G, Kubik-Huch R, Spencer JA, Rockall A. ESUR recommendations for MR imaging of the sonographically indeterminate adnexal mass: an update. *Eur Radiol* 2017;27(6):2248–57. <https://doi.org/10.1007/s00330-016-4600-3>.

- [108] Thomassin-Naggara I, Aubert E, Rockall A, Jalaguier-Coudray A, Rouzier R, Daraï E, Bazot M. Adnexal masses: development and preliminary validation of an MR imaging scoring system. *Radiology* 2013; 267(2):432–43. <https://doi.org/10.1148/radiol.13121161>.
- [109] Turkbey B, Rosenkrantz AB, Haider MA, Padhani AR, Villeirs G, Macura KJ, Tempany CM, Choyke PL, Cornud F, Margolis DJ, Thoeny HC, Verma S, Barentsz J, Weinreb JC. Prostate imaging reporting and data system version 2.1: 2019 update of prostate imaging reporting and data system version 2. *Eur Urol* 2019. <https://doi.org/10.1016/j.eururo.2019.02.033>.
- [110] Gibbs P, Liney GP, Pickles MD, Zelhof B, Rodrigues G, Turnbull LW. Correlation of ADC and T2 measurements with cell density in prostate cancer at 3.0 tesla. *Investig Radiol* 2009;44(9):572–6. <https://doi.org/10.1097/RLI.0b013e3181b4c10e>.
- [111] van As NJ, de Souza NM, Riches SF, Morgan VA, Sohaib SA, Dearnaley DP, Parker CC. A study of diffusion-weighted magnetic resonance imaging in men with untreated localised prostate cancer on active surveillance. *Eur Urol* 2009;56(6):981–7. <https://doi.org/10.1016/j.eururo.2008.11.051>.
- [112] Park YM, Park JS, Yoon HK, Yang WT. Imaging-pathologic correlation of diseases in the axilla. *AJR Am J Roentgenol* 2013;200(2):W130–42. <https://doi.org/10.2214/AJR.12.9259>.
- [113] Katahira K, Takahara T, Kwee TC, Oda S, Suzuki Y, Morishita S, Kitani K, Hamada Y, Kitaoka M, Yamashita Y. Ultra-high-b-value diffusion-weighted MR imaging for the detection of prostate cancer: evaluation in 201 cases with histopathological correlation. *Eur Radiol* 2011;21(1):188–96. <https://doi.org/10.1007/s00330-010-1883-7>.
- [114] Woo S, Suh CH, Kim SY, Cho JY, Kim SH. Head-to-head comparison between high- and standard-b-value DWI for detecting prostate cancer: a systematic review and meta-analysis. *AJR Am J Roentgenol* 2018;210(1):91–100. <https://doi.org/10.2214/AJR.17.18480>.
- [115] Yoshida R, Yoshizako T, Katsube T, Tamaki Y, Ishikawa N, Kitagaki H. Computed diffusion-weighted imaging using 1.5-T magnetic resonance imaging for prostate cancer diagnosis. *Clin Imaging* 2017;41: 78–82. <https://doi.org/10.1016/j.clinimag.2016.10.005>.
- [116] Rosenkrantz AB, Chandarana H, Hindman N, Deng FM, Babb JS, Taneja SS, Geppert C. Computed diffusion-weighted imaging of the prostate at 3 T: impact on image quality and tumour detection. *Eur Radiol* 2013;23(11):3170–7. <https://doi.org/10.1007/s00330-013-2917-8>.
- [117] Shen G, Deng H, Hu S, Jia Z. Comparison of choline-PET/CT, MRI, SPECT, and bone scintigraphy in the diagnosis of bone metastases in patients with prostate cancer: a meta-analysis. *Skelet Radiol* 2014;43(11): 1503–13. <https://doi.org/10.1007/s00256-014-1903-9>.
- [118] Winfield JM, Poillucci G, Blackledge MD, Collins DJ, Shah V, Tunariu N, Kaiser MF, Messiou C. Apparent diffusion coefficient of vertebral haemangiomas allows differentiation from malignant focal deposits in whole-body diffusion-weighted MRI. *Eur Radiol* 2017. <https://doi.org/10.1007/s00330-017-5079-2>.
- [119] Latifoltojar A, Hall-Craggs M, Bainbridge A, Rabin N, Popat R, Rismani A, D'Sa S, Dikaïos N, Sokolska M, Antonelli M, Ourselin S, Yong K, Taylor SA, Halligan S, Punwani S. Whole-body MRI quantitative biomarkers are associated significantly with treatment response in patients with newly diagnosed symptomatic multiple myeloma following bortezomib induction. *Eur Radiol* 2017;27(12):5325–36. <https://doi.org/10.1007/s00330-017-4907-8>.
- [120] Padhani AR, Lecouvet FE, Tunariu N, Koh DM, De Keyzer F, Collins DJ, Sala E, Schlemmer HP, Petralia G, Vargas HA, Fanti S, Tombal HB, de Bono J. METastasis reporting and data system for prostate cancer: practical guidelines for acquisition, interpretation, and reporting of whole-body magnetic resonance imaging-based evaluations of multiorgan involvement in advanced prostate cancer. *Eur Urol* 2017;71(1):81–92. <https://doi.org/10.1016/j.eururo.2016.05.033>.

- [121] Messiou C, Hillengass J, Delorme S, Lecouvet FE, Moulopoulos LA, Collins DJ, Blackledge MD, Abildgaard N, Østergaard B, Schlemmer HP, Landgren O, Asmussen JT, Kaiser MF, Padhani A. Guidelines for acquisition, interpretation, and reporting of whole-body MRI in myeloma: myeloma response assessment and diagnosis system (MY-RADS). *Radiology* 2019;291(1):5–13. <https://doi.org/10.1148/radiol.2019181949>.
- [122] Taylor SA, Mallett S, Ball S, Beare S, Bhatnagar G, Bhowmik A, Boavida P, Bridgewater J, Clarke CS, Duggan M, Ellis S, Glynn-Jones R, Goh V, Groves AM, Hameeduddin A, Janes SM, Johnston EW, Koh DM, Lock S, Miles A, Morris S, Morton A, Navani N, Oliver A, O'Shaughnessy T, Padhani AR, Prezzi D, Punwani S, Quinn L, Rafiee H, Reczko K, Rockall AG, Russell P, Sidhu HS, Strickland N, Tarver K, Teague J, Halligan S, Investigators S. Diagnostic accuracy of whole-body MRI versus standard imaging pathways for metastatic disease in newly diagnosed non-small-cell lung cancer: the prospective streamline L trial. *Lancet Respir Med* 2019;7(6):523–32. [https://doi.org/10.1016/S2213-2600\(19\)30090-6](https://doi.org/10.1016/S2213-2600(19)30090-6).